THE JOURNAL OF PHYSICAL CHEMISTRY Letters

pubs.acs.org/JPCL Letter

First Atomic-Scale Insight into Degradation in Lithium Iron Phosphate Cathodes by Transmission Electron Microscopy

Xing Li,* Fei Jiang, Ke Qu,* Yixian Wang, Yong Pan, Mingshan Wang, Yang Liu, Hao Xu, Junchen Chen, Yun Huang, Jianming Zheng, Peng Gao, Mingyang Chen,* Jiangyu Li, Yong Peng,* and David Mitlin*

Cite This: J. Phys. Chem. Lett. 2020, 11, 4608−4617 Read Online

ACCESS | Metrics & More | Article Recommendations | Supporting Information

ABSTRACT: The capacity-voltage fade phenomenon in lithium iron phosphate ($LiFePO_4$) lithium ion battery cathodes is not understood. We provide its first atomic-scale description, employing advanced transmission electron microscopy combined with electroanalysis and first-principles simulations. Cycling causes near-surface (~30 nm) amorphization of the Olivine crystal structure, with isolated amorphous regions also being present deeper in the bulk crystal. Within this amorphous shell, some of the Fe^{2+} is transformed into Fe^{3+}. Simulations predict that amorphization significantly impedes ion diffusion in $LiFePO_4$ and even more severely in $FePO_4$. The most significant barrier for ion transfer will be in the partially delithiated state due to the presence of $FePO_4$, resulting in the inability to extract the remaining Li^+ and the observed capacity fade. The pyrrole coating suppresses the dissolution of Fe and allows for extended retention of the Olivine structure. It also reduces the level of crossover of iron to the metal anode and stabilizes its solid electrolyte interphase, thus also contributing to the half-cell cycling stability.

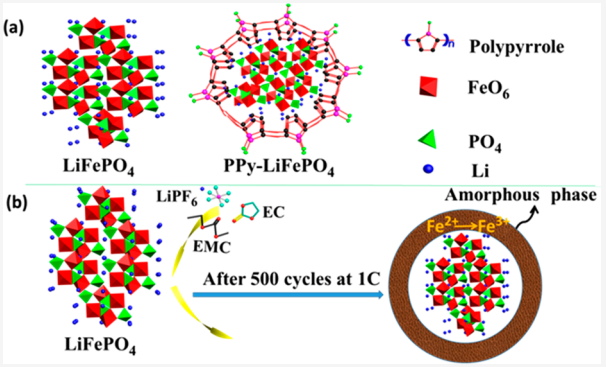

Since the first report in 1997 by Goodenough et al.,[1] lithium iron phosphate ($LiFePO_4$ or LFP) has attracted great interest as a cathode material due to its low cost, superior thermal safety, high reversibility, and acceptable operating voltage (3.45 vs Li^+/Li).[2−8] $LiFePO_4$ has been examined in detail, including by operando X-ray scattering methods that explored the lithiation behavior.[9−18] These analyses provided valuable insight into the equilibrium (i.e., not kinetically limited) lithiation−delithiation phase transformations. However, for large-scale application in electric vehicles (EVs), $LiFePO_4$ faces two critical challenges, both of which may be viewed as kinetic and non-equilibrium in nature. The first key challenge is fast charging,[19,20] where both electronic conductivity and ionic conductivity are necessary.[21,22] Unfortunately, $LiFePO_4$ exhibits both a low electronic conductivity at 10^{-9} S cm^{-1} and a sluggish room-temperature lithium ion diffusion coefficient (D_{Li^+}).[23−25] The second key challenge for LFPs is cycling stability. Cycling-induced Fe dissolution from the cathode is known to be a major problem.[26−30] The dissolved Fe will cross over to the anode and catalytically destabilize the solid electrolyte interphase (SEI).[31−34] To date, the atomic-scale mechanism of capacity decay in $LiFePO_4$ is not documented and serves as a key impediment in advancing both the science and the technology of this cathode material.

Strategies have been developed to improve the electrochemical performance of $LiFePO_4$. These include coating the surface with conductive carbon[35−40] or polymer,[41−44] forming composites with graphene or carbon nanotubes,[45−50] and controlling the particle sizes.[38,51−59] Doping elements and surface modification by metal oxides or conductive phases has also been demonstrated.[60−66] Polypyrrole (PPy) has been reported as one of the most effective LFP coatings, presumably due to its excellent electrical conductivity as well as its nonreactivity with the electrolyte.[67] Importantly, PPy coating is a commercially scalable approach, not requiring major deviations from the well-established LFP cathode fabrication routines. Prior studies have demonstrated that both the rate capability and the cycling stability of $LiFePO_4$ are improved by PPy surface modification.[68,69] The improved rate capability has been primarily ascribed to the highly electrically conductive nature of the PPy coating.[70] However, a mechanistic description of how PPy improves stability is not yet available.[71]

Scheme 1a illustrates the structure of $LiFePO_4$ (LFP) and of polypyrrole (PPy)-coated LFP. Details of the synthesis, analytical, and testing methods are provided in the Methods in the Supporting Information. Figure 1a shows the high-

Received: January 30, 2020
Accepted: May 22, 2020
Published: May 22, 2020

https://dx.doi.org/10.1021/acs.jpclett.0c00317
J. Phys. Chem. Lett. 2020, 11, 4608−4617

Scheme 1. (a) Atomic Structure of As-Synthesized Olivine LFP and of PPy-Coated LFP and (b) Illustration of the Surface Amorphization Process Due to Extended Cycling and the Associated Loss of Fe into the Electrolyte and Ultimately to the Anode

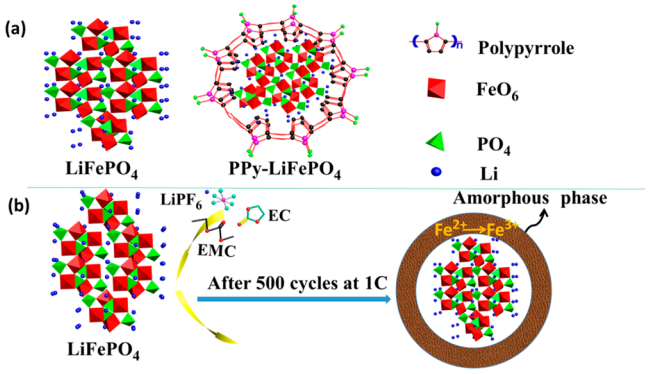

resolution transmission electron microscopy (HRTEM) of the LFP in its as-synthesized state. A 3 nm thick amorphous carbon coating layer on the surface of LFP is observed, agreeing with energy dispersive X-ray spectroscopy (EDS) mapping shown in Figure S1. This carbon coating layer is known to originate from the carbon sources that are part of LFP precursor chemicals.[37] As we will demonstrate, this N-free carbon coating layer will not effectively suppress Fe dissolution, agreeing with prior reports.[33,34] Panels b and c of Figure 1 present the HAADF-STEM micrographs of the surface and subsurface of LFP, respectively. The HAADF image contrast exhibits a relationship of $\sim Z^{1.7}$, with respect to atomic number Z. The LFP crystal in panels b and c of Figure 1 is oriented along the [010] zone axis, making the Olivine crystal structure easy to discern and in agreement with the atomic model shown in Figure 1d. Figure S1a presents the HAADF-STEM image of the as-synthesized LFP and the corresponding EDS elemental mapping of Fe, C, O, and P. It is observed that the LFP exhibits a smooth surface before cycling, with no detectable pitting. The EDS maps also show the uniform distribution of the elements of Fe, C, O, and P without evidence of pitting.

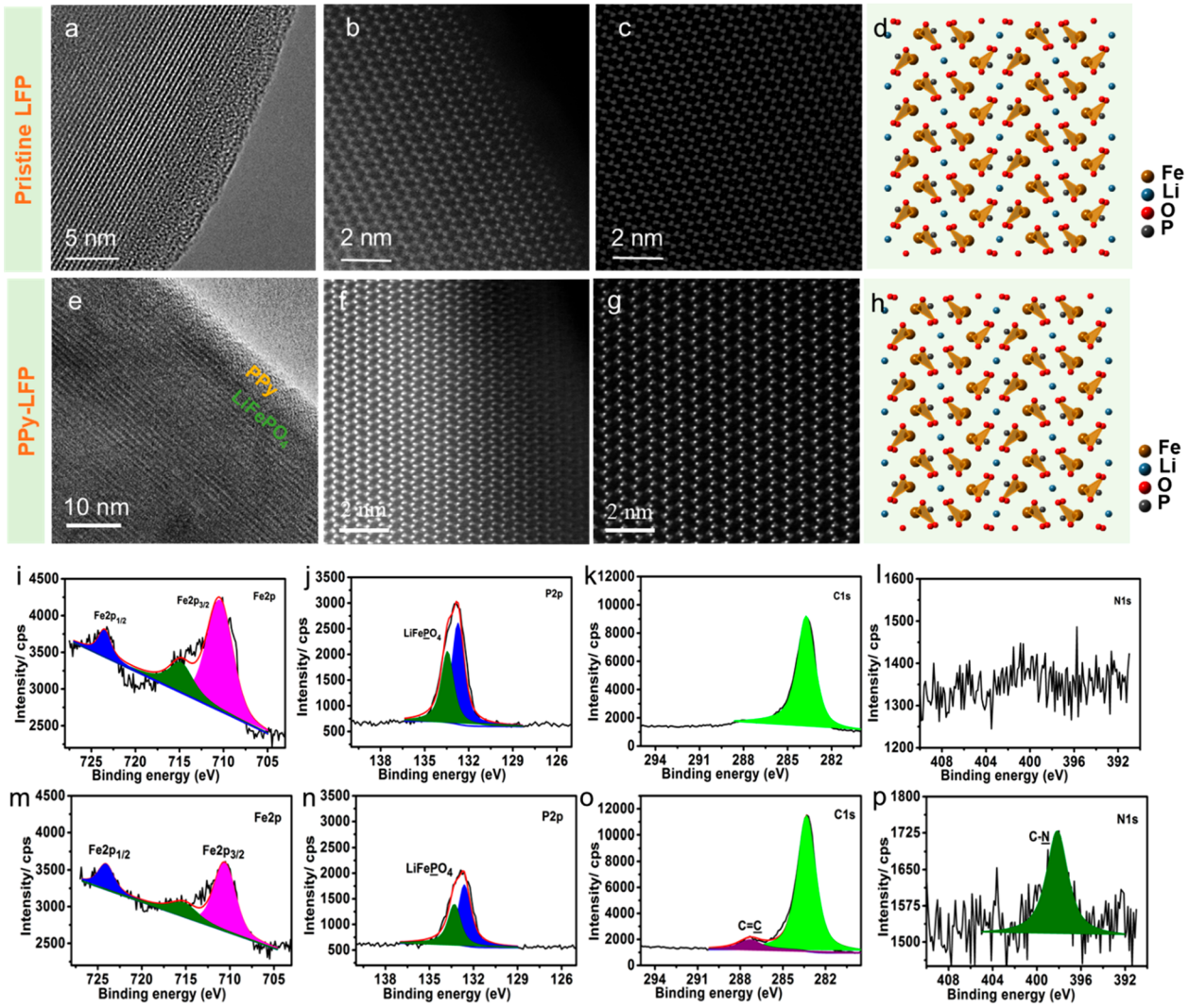

Figure 1. (a) HRTEM of the as-synthesized LFP surface. (b) HAADF-STEM micrographs of LFP surface and (c) bulk, oriented along the [010] zone axis. (d) Atomic model of the Olivine structure of LFP oriented along the [010] zone axis. (e–h) Analogous TEM analysis, but for PPy-LFP. High-resolution XPS spectra of Fe 2p, P 2p, C 1s, and N 1s for pristine LFP (i–l, respectively) and as-synthesized PPy-LFP (m–p, respectively).

https://dx.doi.org/10.1021/acs.jpclett.0c00317
J. Phys. Chem. Lett. 2020, 11, 4608–4617

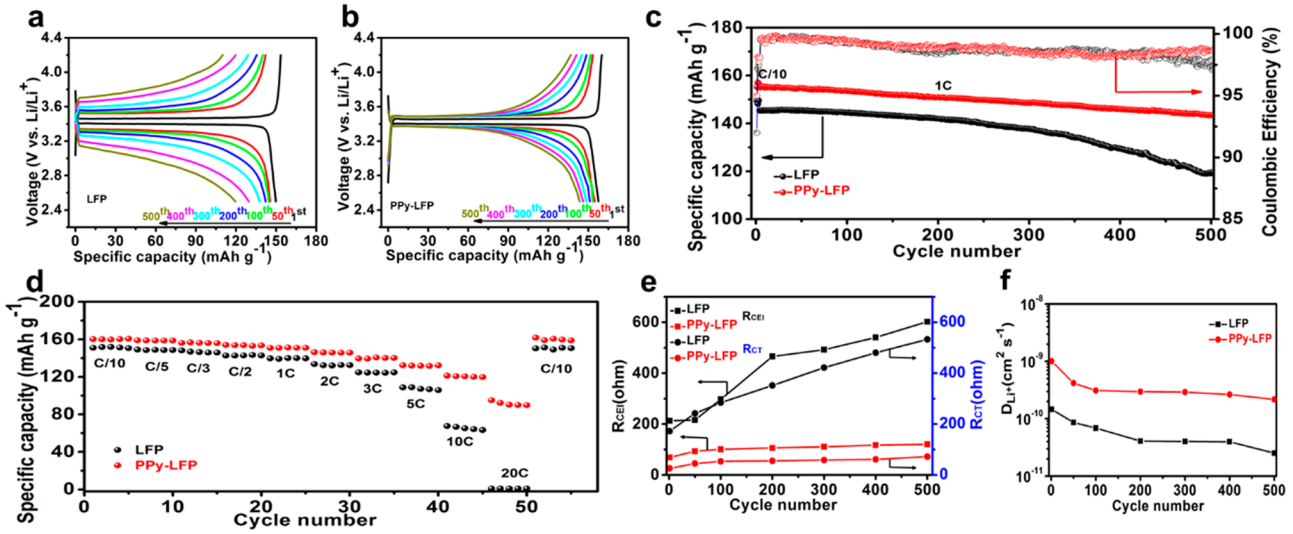

Figure 2. (a and b) Galvanostatic charge−discharge curves of LFP and PPy-LFP, respectively, tested for 500 cycles at 1C (170 mAh g^{-1}) between 2.5 and 4.2 V vs Li/Li^+. (c) Cycling performance of LFP and PPy-LFP at 1C, after three formation cycles at C/10. (d) Master plot showing the rate capability difference in LFP vs PPy-LFP. The associated galvanostatic charge−discharge data are shown in Figure S8. (e) Charge transfer and SEI impedance values obtained from fits of Nyquist plots at different cycles. (f) Solid-state Li^+ diffusivity values obtained from Warburg impedance, as a function of cycle number. The EIS data and analysis are shown in Figures S10 and S11.

Panels e−g of Figure 1 present the HRTEM analysis of as-synthesized PPy-LFP. The distinct PPy coating layer on the LFP surface is visible in Figure 1e. The uniform PPy-LFP coating is ∼9 nm thick. Panels f and g of Figure 1 show the near-surface and bulk structure of the same LFP crystal, with its orientation along the [010] zone axis. The surface and the bulk structure agree with the Olivine phase, per the atomic model shown in Figure 1h. As expected, the PPy coating does not change the near-surface crystal state of the material. Panels a and b of Figure S2 present the HRTEM and HAADF-STEM images of the PPy-LFP. Panels c−f of Figure S2 present energy dispersive X-ray spectroscopy (EDXS) mapping of elements Fe, P, N, and C, respectively. The uniform presence of N element on the surface of PPy-LFP further identifies the successful coating of PPy on LFP. Panels i−l of Figure 1 show the high-resolution X-ray photoelectron spectroscopy (XPS) analysis of as-synthesized LFP. Panels m−p of Figure 1 show the analogous XPS analysis for PPy-LFP. For the high-resolution spectra of Fe 2p, it could be observed that both LFP and PPy-LFP contain the same splitting spectra of Fe $2p_{1/2}$ (724.3 eV) and Fe $2p_{3/2}$ (710.5 eV), agreeing well with the standard XPS spectra of Fe $2p_{3/2}$ in $LiFePO_4$. The peak located at 715.5 eV is the satellite peak of Fe $2p_{3/2}$ in $LiFePO_4$.[72] For the high-resolution spectra of P 2p, it is observed that both LFP and PPy-LFP also contain the same peak splitting. These results further confirm the Olivine $LiFePO_4$ and the PPy coating process does not affect the crystalline structure. For the high-resolution spectra of C 1s and N 1s, it is observed that there are extra peaks with PPy-LFP: C═C in C 1s and C−N in N 1s. These are also associated with the PPy coating in PPy-LFP.[73]

Figure 2 presents the electrochemical performance results for LFP and PPy-LFP cathodes in half-cells, tested at 2.5−4.2 V versus Li/Li^+. Panels a and b of Figure 2 present the galvanostatic charge−discharge curves of LFP and PPy-LFP, respectively, tested for 500 cycles at 1C, with C being the theoretical capacity of 170 mAh g^{-1}. The LFP cathode shows a first reversible (discharge) capacity of 150 mAh g^{-1} at C/10, with a Coulombic efficiency (CE) of 92%. At a 1C rate, its discharge capacity is 145 mAh g^{-1}. The PPy-LFP cathode has an initial capacity of 157 mAh g^{-1} at C/10, with a CE of 95%. This demonstrates that PPy can improve both the reversible capacity and the CE even at the lowest rates. At a 1C rate, the PPy-LFP capacity is 155 mAh g^{-1}, while the baseline LFP is at 145 mAh g^{-1}.

The key major difference between PPy-LFP and baseline LFP is in cycling stability, both in terms of capacity and in terms of voltage retention. According to panels a and b of Figure 2, the combined capacity fade and voltage fade in PPy-LFP remain consistently less severe than in baseline LFP. It is difficult to mechanistically separate the overall capacity fade from the voltage fade. In a degraded structure, diffusional limitations may occur even at low and intermediate C rates. An increasing concentration polarization will reduce the achievable capacity at every cycle while driving up the overpotential required for charge and/or discharge. The two effects, capacity and voltage fade, are therefore inextricably linked. Figure S3 highlights the cycling performance of LFP and PPy-LFP, with PPy contents of 2.3, 5.2, and 8.5 wt %. The 5.2 wt % loading showed optimum performance and was employed for analysis. Figure 2c highlights the cycling performance of LFP and PPy-LFP at 1C, after three formation cycles at C/10. Figure S4 compares the cycling performance of LFP and PPy-LFP at 3C, after three formation cycles at C/10. Figure S5 provides the same comparison at 10C. The raw galvanostatic data for these plots are shown in Figures S6 and S7. Per Figure 2c, after 500 cycles, the reversible capacity of PPy-LFP is 143 mAh g^{-1}, and the corresponding capacity retention rate is 92%. By comparison, after 500 cycles the capacity of LFP is 119 mAh g^{-1}, corresponding to 82% retention.

The second key difference between PPy-LFP and baseline LFP is in rate capability. Figure 2d presents a master plot showing the rate capability difference in LFP versus PPy-LFP. The associated galvanostatic charge−discharge data are shown in Figure S8. It may be observed that at C/3 and above, the PPy-coated electrode displays a higher reversible capacity. The

https://dx.doi.org/10.1021/acs.jpclett.0c00317
J. Phys. Chem. Lett. 2020, 11, 4608−4617

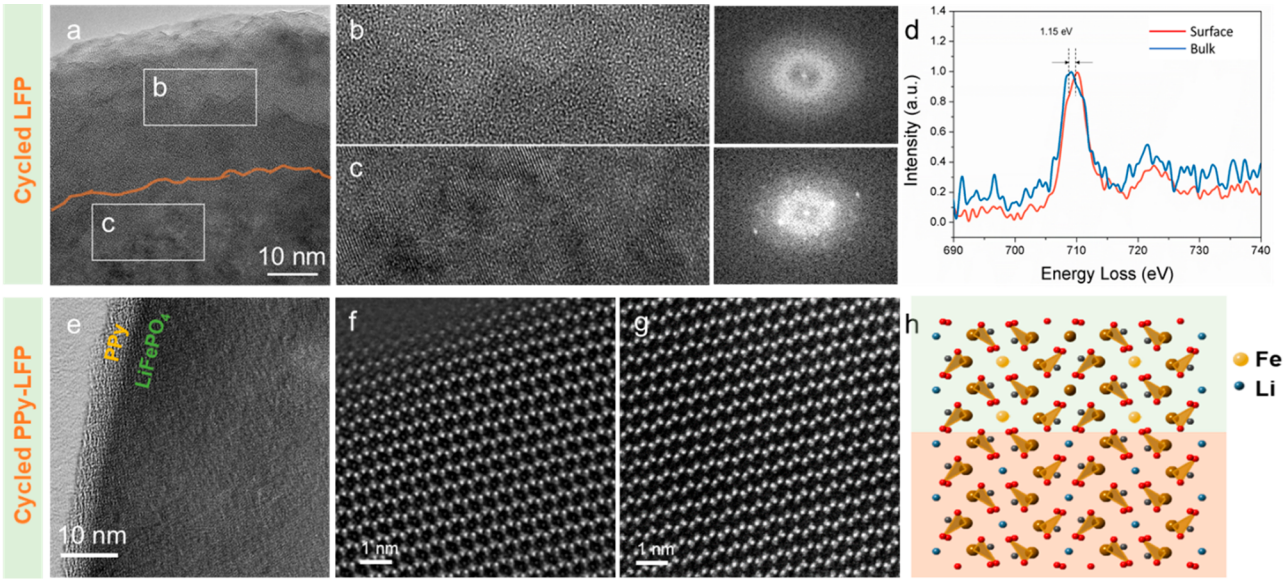

Figure 3. Atomic structure after 500 cycles at 1C. (a) HRTEM images of LFP, with regions for (b) the near surface and (c) bulk identified by rectangles. (d) EELS line scan comparison of near-surface and bulk LFP. (e–g) HAADF-STEM images of the PPy-LFP near-surface and bulk structure. (f) Enlarged micrograph of the PPy-LFP near-surface structure, which remains crystalline but with evidence of Li(Fe) mutual occupation. (g) Structure of bulk PPy-LFP. (h) Atomic models for the Olivine structure in PPy-LFP, comparing near-surface structure (top) to bulk (bottom).

difference between the coated and uncoated becomes more severe at higher currents. For baseline LFP, the reversible capacities at C/10, C/5, C/3, C/2, 1C, 2C, 3C, 5C, 10C, and 20C are 151, 148, 146, 142, 139, 132, 124, 106, 65, and 0.1 (negligible) mAh g^{-1}, respectively. At these C rates, the PPy-LFP reversible capacities are 160, 158, 156, 153, 151, 145, 139, 131, 120, and 92 mAh g^{-1}, respectively. At 20C, the difference between PPy-LFP and baseline LFP is very significant, being 92 mAh g^{-1} versus nil. This indicates the significant difference in the rate capability of the uncoated versus coated specimens is present at early stages. Figure S9 shows the cyclic voltammetry (CV) curves of PPy-LFP and LFP with scan rates ranging from 0.1 to 1 mV s^{-1}. With increasing scan rates, the overpotential is very different for PPy-LFP versus LFP. For baseline LFP, the anodic and cathodic peak differences are 0.320 and 0.984 V, respectively. The corresponding potential differences for PPy-LFP are 0.268 and 0.676 V, respectively.

The enhanced rate capability for PPy-LFP is not just a higher electrical conductivity effect due to the PPy layer. Nitrogen-containing carbons such as PPy do possess higher electrical conductivity than N-free carbons.[74] However, the electrical conductivity of N-free carbon blacks is sufficient for most battery applications. The baseline LFP is covered by nanoscale layer carbon, as well, which means that the rate improvement cannot solely be an electrical effect. As we will show through EIS and GITT, the PPy-LFP electrode possesses a significantly higher Li ion conductivity. Here lies the explanation for the improved rate capability in PPy-LFP versus LFP. An increased Li ion conductivity will lead to a kinetic enhancement at all currents, closer approximating the theoretical capacity at the higher charge rates. Unlike electrical conductance that occurs through the carbon layer, ionic conductance occurs through the bulk of the LFP. The role of PPy is to prevent atomic leaching and associated amorphization in the LFP structure. Per the density functional theory (DFT) calculations shown after the experimental findings, Li ionic diffusion is significantly faster in crystalline LFP than in amorphous LFP. By preventing amorphization, the PPy layer allows the faster Li diffusivity in crystalline LFP to be retained. As we will demonstrate by EIS analysis, the PPY coating is effective in stabilizing the CEI layer on the LFP surface. This also enhances the rate kinetics, allowing for facile charge transfer and Li ion flux through the layer.

The cycled LFP and PPy-LFP cathodes were analyzed using electrochemical impedance spectroscopy (EIS).[75,76] The Nyquist plots contain a semicircle located in the high-frequency region, which correlates to the surface film resistance R_{CEI} and is associated with the CEI/SEI layer.[77−79] The CEI is the cathode electrolyte interphase, while the SEI is the solid electrolyte interphase on the opposing Li metal anode, which would also affect the reaction kinetics of the half-cell. A second semicircle located in a lower-frequency region represents the charge transfer resistance (R_{CT}), being correlated to the reaction control resistance of the primary active material.[80−82] An oblique line located in the low-frequency region represents the Warburg impedance (W), being associated with ion diffusional limitations in the electrode. The intercept at high frequency with the real axis is associated with the electrolyte resistance (R_E), although in strict terms, it also includes a summation of the ohmic resistances of various portions of the cell. The lithium ion diffusion coefficient of LFP and PPy-LFP at cycles 1−500 is calculated from the Warburg impedance coefficient (σ_w) using eqs 1 and 2[83−85]

$$Z_{re} = R_{sf} + R_{ct} + \sigma_w \omega^{-1/2} \quad (1)$$

$$D_{Li} = R^2T^2/(2A^2n^4F^4C^2\sigma_w{}^2) \quad (2)$$

where D_{Li} represents the rate-limiting lithium ion diffusion coefficient, R is the gas constant, T is the absolute temperature, A is the effective area of an electrode, n is the number of electrons transferred, F is the Faraday constant, and C is the concentration of lithium ions. The Warburg impedance coefficient σ_w could be determined from the slope of Z_{re} as a function of $\omega^{-1/2}$, as shown in Figure S10. Panels a and b of Figure S11 present high-frequency portion Nyquist plots for LFP and PPy-LFP, respectively. The inset in each figure shows

https://dx.doi.org/10.1021/acs.jpclett.0c00317
J. Phys. Chem. Lett. 2020, 11, 4608−4617

the equivalent circuit used for fitting the impedance spectra. The impedance spectra were recorded at a charged state of 4.0 V. Figure 2e presents R_{CEI} and R_{CT} values for LFP and PPy-LFP as a function of cycle number. These are also listed in Table S1. It could be observed that the R_{CEI} and R_{CT} values for the PPy-LFP cathodes are dramatically lower than those of the baseline LFP. Therefore, the PPy coating has a major effect in stabilizing both the CEI impedance and the charge transfer impedance during cycling. The nanoscale carbon layer that naturally coats the baseline LFP is not nearly as effective, an observation that may be extrapolated to other carbon coatings that do not contain nitrogen.

The D_{Li} results as a function of cycle number for the two materials are plotted in Figure 2f. The ω is obtained from its relationship with the EIS testing frequency ($\omega = 2\pi f$). Panels a and b of Figure S10 highlight the relationship between the real resistance and the frequency of LFP versus PPy-LFP at the first, 50th, 100th, 200th, 400th, and 500th cycles. The slope is the Warburg impedance and is used to calculate the lithium ion diffusion coefficient D_{Li} with the aid of eq 2. The calculated D_{Li} values for PPy-LFP at the first and 500th cycles are 1.01×10^{-9} and 2.17×10^{-10} cm^2 s^{-1}, respectively. The corresponding calculated D_{Li} values for LFP at the first and 500th cycles are 1.46×10^{-10} and 2.52×10^{-11} cm^2 s^{-1}, respectively. The fact that the values for baseline LFP are an order of magnitude lower than for PPy-LFP provides direct explanation for the major difference in the rate capability between the two materials. The PPy-LFP diffusion coefficient is more stable with cycle number, showing overall less decay than the baseline. It should be noted that the calculated D_{Li} includes the contribution to diffusional resistance through the anode's SEI. Analysis based on a three-electrode cell would have been more favorable in terms of isolating cathode versus anode effects. However, the two-electrode data do give a reasonable holistic picture regarding the role of PPy in the health of the cell.

Cycling-induced structural evolution was characterized at the atomic scale by employing HRTEM and aberration-corrected high-angle annular dark field STEM (HAADF-STEM). Figure 3a shows the HRTEM image of the baseline LFP after 500 cycles at 1C rate. From the enlarged HRTEM images shown in panels b and c of Figure 3, as well as the corresponding fast Fourier transformation (FFT), it is evident that the outer ~30 nm of LFP has fully amorphized. This is illustrated in the schematic panel of Figure S12. It may be observed from panels a and c of Figure 3 that the inner Olivine crystal structure (i.e., more than ~30 nm from surface) now also displays regions of amorphization, indicating that there is bulk degradation in the material. True atomic-resolution HAADF-STEM images of the cycled LFP could not be obtained due to such extensive disorder. Growth of the amorphized regions is correlated with a significant decline in D_{Li} with the cycling of LFP. Per the DFT simulations shown below, amorphization will eliminate the fast [010] Li^+ diffusion path that is present in Olivine. These near-surface amorphization phenomena in cycled LFP and the associated explanation have not been reported previously.

Figure 3d presents the electron energy loss spectroscopy (EELS) line scan of the cycled LFP. There is a drastic difference in the electronic structure of Fe, going from the surface to the bulk. The 1.15 eV larger energy loss in the Fe electronic structure from the near-surface amorphous region demonstrates that it is in a more oxidized state than the Fe^{2+} within the bulk Olivine.[86,87] The more oxidic state of the amorphous Fe exhibits no electrochemical activity,[88] which further contributes to performance loss due to cycling. Figure S13a reports the HAADF-STEM image and the corresponding energy dispersive X-ray spectroscopy (EDS) elemental maps of Fe, O, and P for LFP after 500 electrochemical cycles at a 1C rate. There are two localized regions near the center of the micrograph where Fe has preferentially leached out, leaving behind pits with a dark mass−thickness contrast. The larger pit is substantial enough that it may be resolved in the Fe EDXS map, as well.

Figures S14 and S15 compare survey and high-resolution XPS spectra of the LFP and PPy-LFP cathodes after 500 cycles. Figure S15a shows the high-resolution XPS spectra of Fe 2p. The spectrum shows peak splitting for Fe $2p_{1/2}$ (724.3 eV) and Fe $2p_{3/2}$ (710.5 eV) and the satellite peak of Fe $2p_{3/2}$ (715.5 eV) that belong to $LiFePO_4$.[72] It also contains the Fe $2p_{3/2}$ peak located at 712.5 eV that belongs to $FePO_4$. This further demonstrates that due to electrochemical cycling some Fe^{2+} is transformed to Fe^{3+}, which is known to be inactive.[89−91] PPy-LFP also contains this feature. However, per Figure S15e, PPy-LFP displays a lower relative intensity of Fe^{3+}. This indicates that even in the ~5 nm of the outer surface (approximate depth of the signal), more Fe^{2+} is preserved. This indicates that PPy is effective in suppressing the deleterious transformations and agrees with the electrochemical data. Panels b and f of Figure S15 show the P 2p spectra for LFP and PPy-LFP, respectively. The peak intensity of the P 2p spectrum in $FePO_4$ for PPy-LFP is also lower than that for LFP, agreeing with the Fe 2p signals. One additional difference between the coated and the uncoated material is in the N signal on the PPy-LFP surface, shown in panels d and h of Figure S15. The signal originates from the PPy layer that remains present throughout cycling.

Panels e−g of Figure 3 present HAADF-STEM images of the PPy-LFP structure after 500 cycles at 1C. Figure 3f shows an atomic-resolution image of the near-surface structure, which remains crystalline after 500 cycles. The near-surface crystal structure of PPy-LFP is fundamentally different from that of baseline LFP, the Olivine structure being stabilized. Comparison of the atomic image with the model of the near-surface region, shown in the top half of Figure 3f, indicates that some Li(Fe) mutual occupation has occurred due to cycling.[77,81] In the bulk of the cycled PPy-LFP, there is no evidence of localized amorphization. Per the EDXS mapping shown in Figure S16, there is no evidence of Fe-deficient pits in the PPy-LPF specimens that have been subjected to 500 cycles.

Lithium ion diffusion was simulated employing DFT. Olivine $LiFePO_4$ was compared to amorphized $LiFePO_4$ and to amorphized $FePO_4$, i.e., the material expected in the fully charged state. Figure 4 shows the Li^+ diffusion paths in Olivine $LiFePO_4$ (a), amorphized $FePO_4$ (b, top), and $LiFePO_4$ (b, bottom). For Olivine $LiFePO_4$, the Li^+ diffusion channel along the (010) direction is the most favorable.[92] From nudged elastic band (NEB) calculations, E_{diff} is predicted to be 0.55 eV along the 010 direction, in good agreement with the previous reports of 0.6 eV using MD with GGA function[93] and 0.45 eV using DFT with LDA. The D_{Li} also can be estimated by eq 3.[94]

$$D_{Li} = a^2 \upsilon_0 \exp(-E_{diff}/k_B T) \quad (3)$$

where a is the hopping length (3 Å for Li diffusion) and υ_0 is the corresponding vibrational frequency for Li migration (~10^{12} Hz). The corresponding D_{Li} on Olivine is 4.5×10^{-11} cm^2 s^{-1}.

https://dx.doi.org/10.1021/acs.jpclett.0c00317
J. Phys. Chem. Lett. 2020, 11, 4608−4617

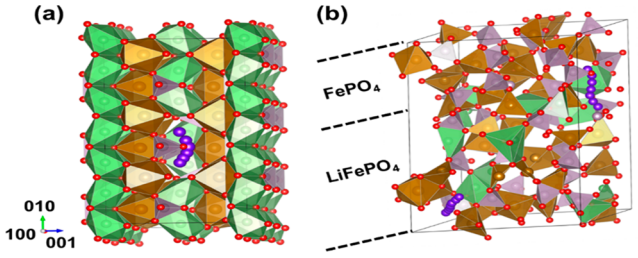

Figure 4. Lithium ion diffusion paths in (a) pristine Olivine $LiFePO_4$ and (b) amorphized $FePO_4$ (top) and $LiFePO_4$ (bottom). Color codes: brown, Fe; gray, P; red, O; green, Li; purple, diffused Li.

In the amorphized $LiFePO_4$, there will be $LiFePO_4$ and $FePO_4$ domains, with their interface playing an important role in Li^+ diffusion. Such an interface is modeled with a layered amorphous supercell comprising a $LiFePO_4$ layer and a $FePO_4$ layer, both shown in Figure 4b. Due to the amorphization, the Li channels are no longer uniformly aligned, and the diffusion rate is no longer simply dependent on a single diffusion barrier. Two diffusion channels in the amorphized $LiFePO_4$ were chosen, one in the $LiFePO_4$ layer, approximately parallel to the interfacial plane, and the other passing through the interface. The E_{diff} for the intra-$LiFePO_4$ diffusion path is 0.74 eV, i.e., ~0.2 eV higher than the E_{diff} for Olivine $LiFePO_4$. The predicted D_{Li} is 2.8×10^{-14} cm^2 s^{-1}, ~3 orders of magnitude slower than with Olivine.

The cross-interface diffusion path from $LiFePO_4$ to $FePO_4$ (4 Å) is found to be longer than the intra-$LiFePO_4$ path (3–3.3 Å). The Li^+ diffusion from $LiFePO_4$ to $FePO_4$ is endothermic by 0.3 eV, in contrast to the intra-$LiFePO_4$ diffusion, which is thermally neutral and symmetric. The cross-interface diffusion path has a forward barrier of 1.23 eV (from $LiFePO_4$ to $FePO_4$), for which the D_{Li} is estimated to be 2.5×10^{-22} cm^2 s^{-1}, indicating that amorphous $FePO_4$ will block Li diffusion. These computational results reveal a clear picture for Li^+ diffusion in $LiFePO_4$. While both amorphized $FePO_4$ and $LiFePO_4$ will block Li^+ diffusion, $FePO_4$ is more detrimental. The most significant barrier for ion transfer will be in the nearly delithiated state, where the amorphous shell is closer to $FePO_4$ and the driving force for further delithiation is low. In this case, the observed capacity fade may be understood as the inability to get the last of the Li^+ out during charging, leading to inactive Li accumulating in the cathode at every cycle. This conclusion agrees well with the observed trends in CE for PPy-LFP versus LFP. While the capacity fade in LFP is substantially worse, the overall trend in the cycling CE values is on par for the two materials. Because the loss of active Li occurs during charge, rather than during discharge, it does not drive down the CE at every cycle. Reduced cycling CE would occur due to the inability to fully strip the Li metal anode and/or relithiate the cathode. The analogous CE values for PPy-LFP and LFP hence strongly suggest that the fade is not anode-driven.

The role of Fe crossover in anode solid electrolyte interphase (SEI) formation was also analyzed. Iron is known to be a potent SEI growth catalyst, leading to cell deterioration.[31−34] Upon leaching out of the LFP cathode during the electrochemical cycling, the Fe cations may diffuse in the electrolyte, pass through the separator, and finally accumulate on the anode surface. This would be directly evident from the analysis of the SEI morphology and chemistry. Figure S17 shows the surface morphologies of the Li metal anodes after the 500 cycles at a 1C rate, panels a and b opposing the LFP cathode and the PPy-LFP cathode, respectively. The Li metal tested against LFP exhibits a

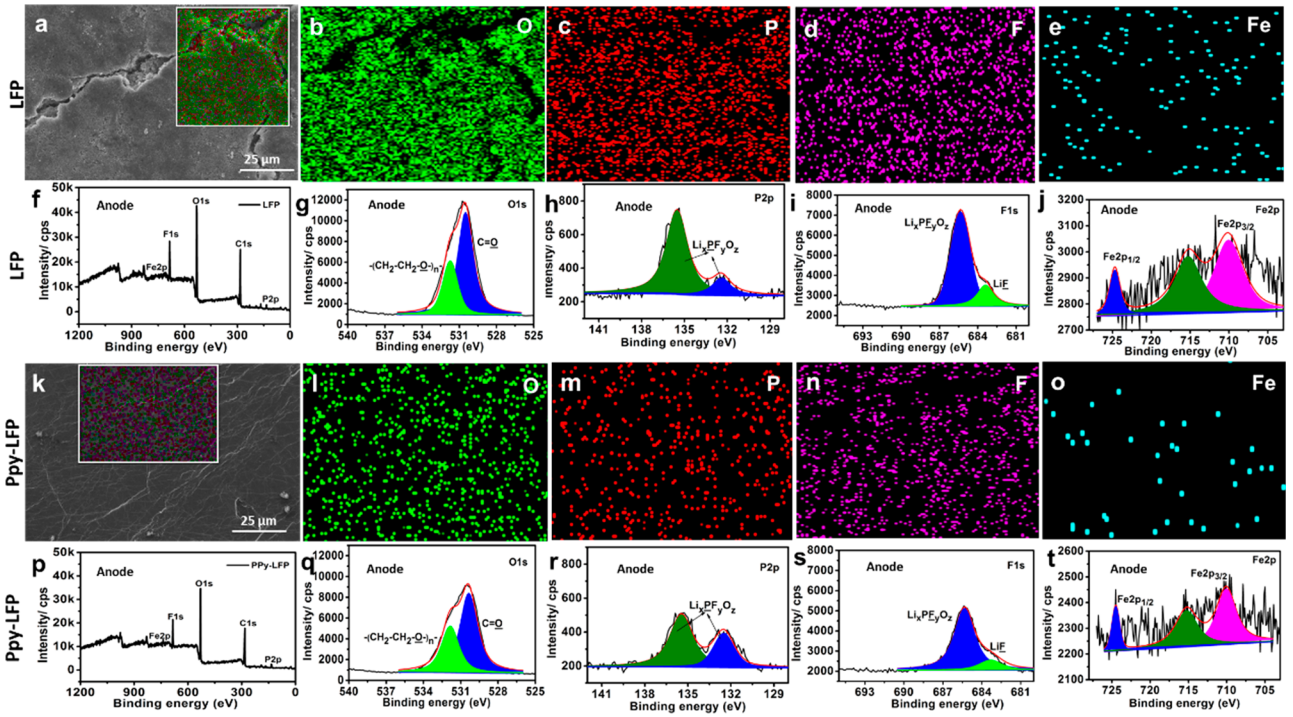

Figure 5. SEM and XPS analysis of Li metal anodes that have been subjected to more than 500 cycles and XPS analysis corresponding to the SEI chemistry. Panels a–j show the anode tested against LFP, and panels k–t show the anode tested against PPy-LFP. SEM analysis shows top down images and EDX elemental mapping of O, P, F, and Fe. XPS spectra shows a survey, Fe 2p, F 1s, P 2p, and O 1s.

https://dx.doi.org/10.1021/acs.jpclett.0c00317
J. Phys. Chem. Lett. 2020, 11, 4608−4617

rough and cracked SEI film surface, while the one tested against PPy-LFP is significantly smoother. A rough and cracked SEI film would increase the interface resistance.[95] Moreover, cracking in the SEI means ongoing exposure of new metal surfaces to the electrolyte.

Panels a–e and k–o of Figure 5 show the EDS mapping of the cycled Li anodes, opposing LFP and PPy-LFP, respectively. It is observed that the amount of Fe on the Li opposing PPy-LFP is smaller than on the Li opposing LFP. This gives further direct evidence that the PPy surface coating reduces the level of Fe dissolution during the electrochemical cycling. Panels f–j and p–t of Figure 5 present the high-resolution XPS spectra of Fe 2p, F 1s, C 1s, and O 1s for the corresponding SEI compositions for the two anodes. The adventitious carbon and hydrocarbon peak is present at 285.0 eV (C–C/C–H). With both LFP and PPy-LFP, the anode SEI films contain the same components, namely, $Li_xPF_yO_z$ (685.4 eV) and LiF (683.5 eV) in F 1s, the carbonyl group [288.7 eV (C═O)] and carbide species (283.0–283.5 eV) in C 1s spectra, and the carbonyl [530.5 eV (C═O)]/ether oxygen [532.0 eV $-(CH_2-CH_2-O)_n-$] in O 1s spectra. These species agree with prior analysis of SEI species on Li metal anodes.[96] The relative peak intensity of Fe 2p within the SEI layer when opposing PPy-LFP is significantly lower than when opposing LFP. This further proves that the PPy surface coating will reduce the level of Fe dissolution during the electrochemical cycling.

To summarize, we provide the conclusive atomic-scale structure-based explanation for the well-known but previously not understood cycling-related performance loss in $LiFePO_4$ cathodes. We also provide a conclusive explanation regarding the role of surface nitrogen-rich carbon coatings (polypyrrole) in reducing the rate at which this performance decay occurs. Employing advanced transmission electron microscopy (TEM) techniques combined with electroanalytical methods and surface science, the following phenomenology is recorded. During cycling, the outer approximately 30 nm of the Olivine $LiFePO_4$ structure is amorphized while some Fe^{2+} is transformed into inactive Fe^{3+}. In addition, localized amorphous regions expand deeper into the material's bulk. Complementary DFT simulation gives insight into how this disordering impedes the necessary diffusion of Li^+, providing a further reason for the observed decrease in capacity, voltage, and rate capability. It is demonstrated that the ∼9 nm-scale layer of polypyrrole minimizes amorphization and reduces the degree of Fe dissolution. In turn, this also weakens the SEI formation tendencies on the Li metal anode where crossed-over Fe catalyzes electrolyte decomposition. These quantitative and holistic findings significantly advance the microstructural design principles for both LFP and for the next generation of cathode materials and coatings.

■ ASSOCIATED CONTENT

Supporting Information

The Supporting Information is available free of charge at https://pubs.acs.org/doi/10.1021/acs.jpclett.0c00317.

Experimental methods, supplementary electrochemical cycling stability, relationship between the real resistance and the frequency (EIS), TEM images, EDX mapping, and TG and FTIR data (PDF)

■ AUTHOR INFORMATION

Corresponding Authors

David Mitlin − *Materials Science and Engineering Program and Texas Materials Institute (TMI), The University of Texas at Austin, Austin, Texas 78712-1591, United States;* orcid.org/0000-0002-7556-3575; Email: David.Mitlin@austin.utexas.edu

Xing Li − *The Center of New Energy Materials and Technology, School of Materials Science and Engineering, Southwest Petroleum University, Chengdu, Sichuan 610500, China;* orcid.org/0000-0003-2745-5673; Email: lixing@swpu.edu.cn

Ke Qu − *Shenzhen Key Laboratory of Nanobiomechanics, Shenzhen Institutes of Advanced Technology, Chinese Academy of Sciences, Shenzhen 518055, China*; Email: ke.qu@siat.ac.cn

Mingyang Chen − *Center for Green Innovation, School of Materials Science and Engineering, University of Science and Technology Beijing, Beijing 100083, China;* orcid.org/0000-0002-9866-8695; Email: mychen@ustb.edu.cn

Yong Peng − *Key Laboratory of Magnetism and Magnetic Materials of the Ministry of Education, School of Physical Science and Technology and Electron Microscopy Centre of Lanzhou University, Lanzhou University, Lanzhou 730000, P. R. China;* orcid.org/0000-0002-6980-4694; Email: pengy@lzu.edu.cn

Authors

Fei Jiang − *The Center of New Energy Materials and Technology, School of Materials Science and Engineering, Southwest Petroleum University, Chengdu, Sichuan 610500, China*

Yixian Wang − *Materials Science and Engineering Program and Texas Materials Institute (TMI), The University of Texas at Austin, Austin, Texas 78712-1591, United States;* orcid.org/0000-0001-6107-8352

Yong Pan − *The Center of New Energy Materials and Technology, School of Materials Science and Engineering, Southwest Petroleum University, Chengdu, Sichuan 610500, China;* orcid.org/0000-0001-5689-3598

Mingshan Wang − *The Center of New Energy Materials and Technology, School of Materials Science and Engineering, Southwest Petroleum University, Chengdu, Sichuan 610500, China;* orcid.org/0000-0001-5461-3951

Yang Liu − *The Center of New Energy Materials and Technology, School of Materials Science and Engineering, Southwest Petroleum University, Chengdu, Sichuan 610500, China*

Hao Xu − *The Center of New Energy Materials and Technology, School of Materials Science and Engineering, Southwest Petroleum University, Chengdu, Sichuan 610500, China*

Junchen Chen − *The Center of New Energy Materials and Technology, School of Materials Science and Engineering, Southwest Petroleum University, Chengdu, Sichuan 610500, China*

Yun Huang − *The Center of New Energy Materials and Technology, School of Materials Science and Engineering, Southwest Petroleum University, Chengdu, Sichuan 610500, China*

Jianming Zheng − *College of Chemistry and Chemical Engineering, Xiamen University, Xiamen 361005, China*

Peng Gao − *International Center for Quantum Materials and Electron Microscopy Laboratory, School of Physics, Peking*

https://dx.doi.org/10.1021/acs.jpclett.0c00317
J. Phys. Chem. Lett. 2020, 11, 4608−4617

University, Beijing 100871, China; orcid.org/0000-0003-0860-5525

Jiangyu Li − *Shenzhen Key Laboratory of Nanobiomechanics, Shenzhen Institutes of Advanced Technology, Chinese Academy of Sciences, Shenzhen 518055, China;* orcid.org/0000-0003-0533-1397

Complete contact information is available at: https://pubs.acs.org/10.1021/acs.jpclett.0c00317

Notes

The authors declare no competing financial interest.

■ ACKNOWLEDGMENTS

This work was supported by the National Natural Science Foundation of China (Grant 51502250) and the Science & Technology Department of Sichuan Province (Grants 2017JQ0044 and 2019-GH02-00052-HZ). D.M. and Y.W. (guidance and interpretation of research and preparation of the manuscript) were supported by the National Science Foundation, Division of Materials Research, Award 1938833.

■ REFERENCES

(1) Padhi, A. K.; Nanjundaswamy, K. S.; Goodenough, J. B. Phospho-olivines as positive-electrode materials for rechargeable lithium batteries. *J. Electrochem. Soc.* **1997**, *144*, 1188−1194.

(2) Wang, Y.; He, P.; Zhou, H. Olivine $LiFePO_4$: Development and future. *Energy Environ. Sci.* **2011**, *4*, 805−817.

(3) Li, D.; Zhou, H. Two-phase transition of Li-intercalation compounds in Li-ion batteries. *Mater. Today* **2014**, *17*, 451−463.

(4) Goodenough, J. B.; Park, K.-S. The Li-ion rechargeable battery: A perspective. *J. Am. Chem. Soc.* **2013**, *135*, 1167−1176.

(5) Yuan, L.-X.; Wang, Z.-H.; Zhang, W.-X.; Hu, X.-L.; Chen, J.-T.; Huang, Y.-H.; Goodenough, J. B. Development and challenges of $LiFePO_4$ cathode material for lithium-ion batteries. *Energy Environ. Sci.* **2011**, *4*, 269−284.

(6) Ravet, N.; Chouinard, Y.; Magnan, J. F.; Besner, S.; Gauthier, M.; Armand, M. Electroactivity of natural and synthetic triphylite. *J. Power Sources* **2001**, *97*−*98*, 503−507.

(7) Devaraju, M. K.; Honma, I. Hydrothermal and solvothermal process towards development of $LiMPO_4$ (M = Fe, Mn) nanomaterials for lithium-ion batteries. *Adv. Energy Mater.* **2012**, *2*, 284−297.

(8) Singh, D. P.; Mulder, F. M.; Abdelkader, A. M.; Wagemaker, M. Facile micro templating $LiFePO_4$ electrodes for high performance Li-ion batteries. *Adv. Energy Mater.* **2013**, *3*, 572−578.

(9) Lim, J.; Li, Y.; Alsem, D. H.; So, H.; Lee, S. C.; Bai, P.; Cogswell, D. A.; Liu, X.; Jin, N.; Yu, Y.-S.; et al. Origin and hysteresis of lithium compositional spatiodynamics within battery primary particles. *Science* **2016**, *353*, 566−571.

(10) Wang, J.; Chen-Wiegart, Y.-c. K.; Wang, J. In operando tracking phase transformation evolution of lithium iron phosphate with hard X-ray microscopy. *Nat. Commun.* **2014**, *5*, 4570.

(11) Li, Y.; Weker, J. N.; Gent, W. E.; Mueller, D. N.; Lim, J.; Cogswell, D. A.; Tyliszczak, T.; Chueh, W. C. Dichotomy in the lithiation pathway of ellipsoidal and platelet $LiFePO_4$ particles revealed through nanoscale operando state-of-charge imaging. *Adv. Funct. Mater.* **2015**, *25*, 3677−3687.

(12) Ohmer, N.; Fenk, B.; Samuelis, D.; Chen, C.-C.; Maier, J.; Weigand, M.; Goering, E.; Schütz, G. Phase evolution in single-crystalline $LiFePO_4$ followed by in situ scanning X-ray microscopy of a micrometre-sized battery. *Nat. Commun.* **2015**, *6*, 6045.

(13) Li, L.; Chen-Wiegart, Y.-c. K.; Wang, J.; Gao, P.; Ding, Q.; Yu, Y.-S.; Wang, F.; Cabana, J.; Wang, J.; Jin, S. Visualization of electrochemically driven solid-state phase transformations using operando hard X-ray spectro-imaging. *Nat. Commun.* **2015**, *6*, 6883.

(14) Orikasa, Y.; Gogyo, Y.; Yamashige, H.; Katayama, M.; Chen, K. Z.; Mori, T.; Yamamoto, K.; Masese, T.; Inada, Y.; Ohta, T.; et al. Ionic conduction in lithium ion battery composite electrode governs cross-sectional reaction distribution. *Sci. Rep.* **2016**, *6*, 26382.

(15) Xiang, K.; Yang, K.; Carter, W. C.; Tang, M.; Chiang, Y.-M. Mesoscopic phase transition kinetics in secondary particles of electrode-active materials in lithium-ion batteries. *Chem. Mater.* **2018**, *30*, 4216−4225.

(16) Paolella, A.; Turner, S.; Bertoni, G.; Hovington, P.; Flacau, R.; Boyer, C.; Feng, Z.; Colombo, M.; Marras, S.; Prato, M.; et al. Accelerated removal of Fe-antisite defects while nanosizing hydrothermal $LiFePO_4$ with Ca^{2+}. *Nano Lett.* **2016**, *16*, 2692−2697.

(17) Chen, J.; Graetz, J. Study of antisite defects in hydrothermally prepared $LiFePO_4$ by in situ X-ray diffraction. *ACS Appl. Mater. Interfaces* **2011**, *3*, 1380−1384.

(18) Johnson, I. D.; Ashton, T. E.; Blagovidova, E.; Smales, G. J.; Lübke, M.; Baker, P. J.; Corr, S. A.; Darr, J. A. Mechanistic insights of Li^+diffusion within doped $LiFePO_4$ from muon spectroscopy. *Sci. Rep.* **2018**, *8*, 4114.

(19) Zaghib, K.; Dontigny, M.; Guerfi, A.; Charest, P.; Rodrigues, I.; Mauger, A.; Julien, C. M. Safe and fast-charging Li-ion battery with long shelf life for power applications. *J. Power Sources* **2011**, *196*, 3949−3954.

(20) Hu, J.; Li, W.; Duan, Y.; Cui, S.; Song, X.; Liu, Y.; Zheng, J.; Lin, Y.; Pan, F. Single-particle performances and properties of $LiFePO_4$ nanocrystals for Li-ion batteries. *Adv. Energy Mater.* **2017**, *7*, 1601894.

(21) Wang, J.; Sun, X. Olivine $LiFePO_4$: The remaining challenges for future energy storage. *Energy Environ. Sci.* **2015**, *8*, 1110−1138.

(22) Wang, G.; Liu, H.; Liu, J.; Qiao, S.; Lu, G.; Munroe, P.; Ahn, H. Mesoporous $LiFePO_4$/C nanocomposite cathode materials for high power lithium ion batteries with superior performance. *Adv. Mater.* **2010**, *22*, 4944−4948.

(23) Malik, R.; Burch, D.; Bazant, M.; Ceder, G. Particle size dependence of the ionic diffusivity. *Nano Lett.* **2010**, *10*, 4123−4127.

(24) Laffont, L.; Delacourt, C.; Gibot, P.; Wu, M. Y.; Kooyman, P.; Masquelier, C.; Tarascon, J. M. Study of the $LiFePO_4$/$FePO_4$ two-phase system by high-resolution electron energy loss spectroscopy. *Chem. Mater.* **2006**, *18*, 5520−5529.

(25) Morgan, D.; Van der Ven, A.; Ceder, G. Li conductivity in $LixMPO_4$ (M = Mn, Fe, Co, Ni) olivine materials. *Electrochem. Solid-State Lett.* **2004**, *7*, A30−A32.

(26) Mauger, A.; Julien, C. Surface modifications of electrode materials for lithium-ion batteries: Status and trends. *Ionics* **2014**, *20*, 751−787.

(27) Safari, M.; Delacourt, C. Aging of a commercial graphite/$LiFePO_4$ cell. *J. Electrochem. Soc.* **2011**, *158*, A1123−A1135.

(28) Zhang, Y.; Wang, C.-Y.; Tang, X. Cycling degradation of an automotive $LiFePO_4$ lithium-ion battery. *J. Power Sources* **2011**, *196*, 1513−1520.

(29) Julien, C. M.; Mauger, A.; Zaghib, K. Surface effects on electrochemical properties of nano-sized $LiFePO_4$. *J. Mater. Chem.* **2011**, *21*, 9955−9968.

(30) Wang, J.; Yang, J.; Tang, Y.; Li, R.; Liang, G.; Sham, T.-K.; Sun, X. Surface aging at olivine $LiFePO_4$: A direct visual observation of iron dissolution and the protection role of nano-carbon coating. *J. Mater. Chem. A* **2013**, *1*, 1579−1586.

(31) Zaghib, K.; Ravet, N.; Gauthier, M.; Gendron, F.; Mauger, A.; Goodenough, J. B.; Julien, C. M. Optimized electrochemical performance of $LiFePO_4$ at 60°C with purity controlled by SQUID magnetometry. *J. Power Sources* **2006**, *163*, 560−566.

(32) Amine, K.; Liu, J.; Kang, S.; Belharouak, I.; Hyung, Y.; Vissers, D.; Henriksen, G. Improved lithium manganese oxide spinel/graphite Li-ion cells for high-power applications. *J. Power Sources* **2004**, *129*, 14−19.

(33) Song, G.-M.; Wu, Y.; Xu, Q.; Liu, G. Enhanced electrochemical properties of $LiFePO_4$ cathode for Li-ion batteries with amorphous NiP coating. *J. Power Sources* **2010**, *195*, 3913−3917.

(34) Amine, K.; Liu, J.; Belharouak, I. High-temperature storage and cycling of C-$LiFePO_4$/graphite Li-ion cells. *Electrochem. Commun.* **2005**, *7*, 669−673.

(35) Liu, Y.; Liu, J.; Wang, J.; Banis, M. N.; Xiao, B.; Lushington, A.; Xiao, W.; Li, R.; Sham, T.-K.; Liang, G.; Sun, X. Formation of size-dependent and conductive phase on lithium iron phosphate during carbon coating. *Nat. Commun.* **2018**, *9*, 929.
(36) Zaghib, K.; Mauger, A.; Gendron, F.; Julien, C. M. Surface effects on the physical and electrochemical properties of thin $LiFePO_4$ particles. *Chem. Mater.* **2008**, *20*, 462−469.
(37) Liu, Y.; Wang, J.; Liu, J.; Banis, M. N.; Xiao, B.; Lushington, A.; Xiao, W.; Li, R.; Sham, T.-K.; Liang, G.; et al. Origin of phase inhomogeneity in lithium iron phosphate during carbon coating. *Nano Energy* **2018**, *45*, 52−60.
(38) Wang, Y.; Wang, Y.; Hosono, E.; Wang, K.; Zhou, H. The design of a $LiFePO_4$/carbon nanocomposite with a core-shell structure and its synthesis by an in situ polymerization restriction method. *Angew. Chem.* **2008**, *120*, 7571−7557.
(39) Wang, B.; Liu, T.; Liu, A.; Liu, G.; Wang, L.; Gao, T.; Wang, D.; Zhao, X. A hierarchical porous C@$LiFePO_4$/carbon nanotubes microsphere composite for high-rate lithium-ion batteries: Combined experimental and theoretical study. *Adv. Energy Mater.* **2016**, *6*, 1600426.
(40) Oh, S. W.; Myung, S.-T.; Oh, S.-M.; Oh, K.-H.; Amine, K.; Scrosati, B.; Sun, Y.-K. Double carbon coating of $LiFePO_4$ as high rate electrode for rechargeable lithium batteries. *Adv. Mater.* **2010**, *22*, 4842−4845.
(41) Wilcox, J. D.; Doeff, M. M.; Marcinek, M.; Kostecki, R. Factors influencing the quality of carbon coatings on $LiFePO_4$. *J. Electrochem. Soc.* **2007**, *154*, A389−A395.
(42) Wang, Y.; Mei, R.; Yang, X. Enhanced electrochemical properties of $LiFePO_4$/C synthesized with two kinds of carbon sources, PEG-4000 (organic) and super p (inorganic). *Ceram. Int.* **2014**, *40*, 8439−8444.
(43) Ponrouch, A.; Goni, A. R.; Sougrati, M. T.; Ati, M.; Tarascon, J.-M.; Nava-Avendano, J.; Palacin, M. R. A new room temperature and solvent free carbon coating procedure for battery electrode materials. *Energy Environ. Sci.* **2013**, *6*, 3363−3371.
(44) Yoon, S.; Liao, C.; Sun, X.-G.; Bridges, C. A.; Unocic, R. R.; Nanda, J.; Dai, S.; Paranthaman, M. P. Conductive surface modification of $LiFePO_4$ with nitrogen-doped carbon layers for lithium-ion batteries. *J. Mater. Chem.* **2012**, *22*, 4611−4614.
(45) Wei, W.; Lv, W.; Wu, M.-B.; Su, F.-Y.; He, Y.-B.; Li, B.; Kang, F.; Yang, Q.-H. The effect of graphene wrapping on the performance of $LiFePO_4$ for a lithium ion battery. *Carbon* **2013**, *57*, 530−536.
(46) Zhou, Y.; Wang, J.; Hu, Y.; O'Hayre, R.; Shao, Z. A porous $LiFePO_4$ and carbon nanotube composite. *Chem. Commun.* **2010**, *46*, 7151−7153.
(47) Liu, J.; Banis, M. N.; Sun, Q.; Lushington, A.; Li, R.; Sham, T.-K.; Sun, X. Rational design of atomic-layer-deposited $LiFePO_4$ as a high-performance cathode for lithium-ion batteries. *Adv. Mater.* **2014**, *26*, 6472−6477.
(48) Wang, B.; Al Abdulla, W.; Wang, D.; Zhao, X. A three-dimensional porous $LiFePO_4$ cathode material modified with a nitrogen-doped graphene aerogel for high-power lithium ion batteries. *Energy Environ. Sci.* **2015**, *8*, 869−875.
(49) Ding, J.; Zhang, H.; Zhou, H.; Feng, J.; Zheng, X.; Zhong, C.; Paek, E.; Hu, W.; Mitlin, D. Sulfur-grafted hollow carbon spheres for potassium-ion battery anodes. *Adv. Mater.* **2019**, *31*, 1900429.
(50) Wu, Y. M.; Wen, Z. H.; Li, J. H. Hierarchical carbon-coated $LiFePO_4$ nanoplate microspheres with high electrochemical performance for Li-ion batteries. *Adv. Mater.* **2011**, *23*, 1126−1129.
(51) Lotfabad, E. M.; Ding, J.; Cui, K.; Kohandehghan, A.; Kalisvaart, W. P.; Hazelton, M.; Mitlin, D. High-density sodium and lithium ion battery anodes from banana peels. *ACS Nano* **2014**, *8*, 7115−7129.
(52) Yu, F.; Lim, S. H.; Zhen, Y.; An, Y.; Lin, J. Optimized electrochemical performance of three-dimensional porous $LiFePO_4$/C microspheres via microwave irradiation assisted synthesis. *J. Power Sources* **2014**, *271*, 223−230.
(53) Jiang, Y.; Liao, S.; Liu, Z.; Xiao, G.; Liu, Q.; Song, H. High performance $LiFePO_4$ microsphere composed of nanofibers with an alcohol-thermal approach. *J. Mater. Chem. A* **2013**, *1*, 4546−4551.
(54) Li, Z.; Peng, Z.; Zhang, H.; Hu, T.; Hu, M.; Zhu, K.; Wang, X. [100]-oriented $LiFePO_4$ nanoflakes toward high rate Li-ion battery cathode. *Nano Lett.* **2016**, *16*, 795−799.
(55) Liu, J.; Conry, T. E.; Song, X.; Doeff, M. M.; Richardson, T. J. Nanoporous spherical $LiFePO_4$ for high performance cathodes. *Energy Environ. Sci.* **2011**, *4*, 885−888.
(56) Wang, B.; Xie, Y.; Liu, T.; Luo, H.; Wang, B.; Wang, C.; Wang, L.; Wang, D.; Dou, S.; Zhou, Y. $LiFePO_4$ quantum-dots composite synthesized by a general microreactor strategy for ultra-high-rate lithium ion batteries. *Nano Energy* **2017**, *42*, 363−372.
(57) Wang, L.; He, X.; Sun, W. T.; Wang, J.; Li, Y.; Fan, S. Crystal orientation tuning of $LiFePO_4$ nanoplates for high rate lithium battery cathode materials. *Nano Lett.* **2012**, *12*, 5632−5636.
(58) Chung, S.-Y.; Kim, J.-G.; Kim, Y.-M.; Lee, Y.-B. Three-dimensional morphology of iron phosphide phases in a polycrystalline LiFePO4 matrix. *Adv. Mater.* **2011**, *23*, 1398−1403.
(59) Teng, F.; Santhanagopalan, S.; Asthana, A.; Geng, X.; Mho, S.-i.; Shahbazian-Yassar, R.; Meng, D. D. Self-assembly of LiFePO4 nanodendrites in a novel system of ethylene glycol−water. *J. Cryst. Growth* **2010**, *312*, 3493−3502.
(60) Ravet, N.; Abouimrane, A.; Armand, M. On the electronic conductivity of phospho-olivines as lithium storage electrodes. *Nat. Mater.* **2003**, *2*, 702.
(61) Meethong, N.; Kao, Y.-H.; Carter, W. C.; Chiang, Y.-M. Comparative study of lithium transport kinetics in olivine cathodes for Li-ion batteries. *Chem. Mater.* **2010**, *22*, 1088−1097.
(62) Moretti, A.; Giuli, G.; Nobili, F.; Trapananti, A.; Aquilanti, G.; Tossici, R.; Marassi, R. Structural and electrochemical characterization of vanadium-doped $LiFePO_4$ cathodes for lithium-ion batteries. *J. Electrochem. Soc.* **2013**, *160*, A940−A949.
(63) Herle, P. S.; Ellis, B.; Coombs, N.; Nazar, L. F. Nano-network electronic conduction in iron and nickel olivione phosphates. *Nat. Mater.* **2004**, *3*, 147−152.
(64) Ban, C.; Yin, W.-J.; Tang, H.; Wei, S.-H.; Yan, Y.; Dillon, A. C. A novel codoping approach for enhancing the performance of $LiFePO_4$ cathodes. *Adv. Energy Mater.* **2012**, *2*, 1028−1032.
(65) Omenya, F.; Wen, B.; Fang, J.; Zhang, R.; Wang, Q.; Chernova, N. A.; Schneider-Haefner, J.; Cosandey, F.; Whittingham, M. S. Mg substitution clarifies the reaction mechanism of olivine $LiFePO_4$. *Adv. Energy Mater.* **2015**, *5*, 1401204.
(66) Koenig, G. M.; Ma, J.; Key, B.; Fink, J.; Low, K.-B.; Shahbazian-Yassar, R.; Belharouak, I. Composite of $LiFePO_4$ with Titanium Phosphate Phases as Lithium-Ion Battery Electrode Material. *J. Phys. Chem. C* **2013**, *117*, 21132−21138.
(67) Boyano, I.; Blazquez, J. A.; de Meatza, I.; Bengoechea, M.; Miguel, O.; Grande, H.; Huang, Y. H.; Goodenough, J. B. Preparation of C-$LiFePO_4$/polypyrrole lithium rechargeable cathode by consecutive potential steps electrodeposition. *J. Power Sources* **2010**, *195*, 5351−5359.
(68) Wang, G.; Yang, L.; Chen, Y.; Wang, J.; Bewlay, S.; Liu, H. An investigation of polypyrrole-$LiFePO_4$ composite cathode materials for lithium-ion batteries. *Electrochim. Acta* **2005**, *50*, 4649−4654.
(69) Wang, J.-Z.; Chou, S.-L.; Chen, J.; Chew, S.-Y.; Wang, G.-X.; Konstantinov, K.; Wu, J.; Dou, S.-X.; Liu, H. K. Paper-like free-standing polypyrrole and polypyrrole−$LiFePO_4$ composite films for flexible and bendable rechargeable battery. *Electrochem. Commun.* **2008**, *10*, 1781−1784.
(70) Yang, Y.; Liao, X.-Z.; Ma, Z.-F.; Wang, B.-F.; He, L.; He, Y.-S. Superior high-rate cycling performance of $LiFePO_4$/C-PPy composite at 55°C. *Electrochem. Commun.* **2009**, *11*, 1277−1280.
(71) Hu, E.; Yu, X.; Lin, R.; Bi, X.; Lu, J.; Bak, S.; Nam, K.-W.; Xin, H. L.; Jaye, C.; Fischer, D. A.; et al. Evolution of redox couples in Li- and Mn-rich cathode materials and mitigation of voltage fade by reducing oxygen release. *Nat. Energy* **2018**, *3*, 690−698.

https://dx.doi.org/10.1021/acs.jpclett.0c00317
J. Phys. Chem. Lett. 2020, 11, 4608−4617

(72) Tu, J.; Wu, K.; Tang, H.; Zhou, H.; Jiao, S. Mg−Ti co-doping behavior of porous $LiFePO_4$ microspheres for high-rate lithium-ion batteries. *J. Mater. Chem. A* **2017**, *5*, 17021−17028.
(73) Dubal, D. P.; Caban-Huertas, Z.; Holze, R.; Gomez-Romero, P. Growth of polypyrrole nanostructures through reactive templates for energy storage applications. *Electrochim. Acta* **2016**, *191*, 346−354.
(74) Pollak, E.; Salitra, G.; Soffer, A.; Aurbach, D. On the reaction of oxygen with nitrogen-containing and nitrogen-free carbons. *Carbon* **2006**, *44*, 3302−3307.
(75) Markevich, E.; Fridman, K.; Sharabi, R.; Elazari, R.; Salitra, G.; Gottlieb, H. E.; Gershinsky, G.; Garsuch, A.; Semrau, G.; Schmidt, M. A.; et al. Amorphous columnar silicon anodes for advanced high voltage lithium ion full cells: Dominant factors governing cycling performance. *J. Electrochem. Soc.* **2013**, *160*, A1824−A1833.
(76) Li, Z.; Zhang, J.; Lu, Y.; Lou, X. W. D. A pyrolyzed polyacrylonitrile/selenium disulfide composite cathode with remarkable lithium and sodium storage performances. *Sci. Advances* **2018**, *4*, eaat1687.
(77) Li, X.; Zhang, K.; Mitlin, D.; Paek, E.; Wang, M.; Jiang, F.; Huang, Y.; Yang, Z.; Gong, Y.; Gu, L.; et al. Li-rich Li-$[Li_{1/6}Fe_{1/6}Ni_{1/6}Mn_{1/2}]O_2$ (LFNMO) cathodes: Atomic scale insight on the mechanisms of cycling decay and of the improvement due to cobalt phosphate surface modification. *Small* **2018**, *14*, 1802570.
(78) Zhang, Y.; Sun, Y.; Peng, L.; Yang, J.; Jia, H.; Zhang, Z.; Shan, B.; Xie, J. Se as eutectic accelerator in sulfurized polyacrylonitrile for high performance all-solid-state lithium-sulfur battery. *Energy Storage Mater.* **2019**, *21*, 287−296.
(79) Pham-Cong, D.; Choi, J. H.; Yun, J.; Bandarenka, A. S.; Kim, J.; Braun, P. V.; Jeong, S. Y.; Cho, C. R. Synergistically enhanced electrochemical performance of hierarchical $MoS_2/TiNb_2O_7$ heteronanostructures as anode materials for Li-ion batteries. *ACS Nano* **2017**, *11*, 1026−1033.
(80) Tian, M.; Pei, F.; Yao, M.; Fu, Z.; Lin, L.; Wu, G.; Xu, G.; Kitagawa, H.; Fang, X. Ultrathin MOF nanosheet assembled highly oriented microporous membrane as an interlayer for lithium-sulfur batteries. *Energy Storage Mater.* **2019**, *21*, 14−21.
(81) Li, X.; Zhang, K.; Wang, M.; Liu, Y.; Qu, M.; Zhao, W.; Zheng, J. Dual functions of zirconium modification on improving the electrochemical performance of Ni-rich $LiNi_{0.8}Co_{0.1}Mn_{0.1}O_2$. *Sustain. Energy Fuels* **2018**, *2*, 413−421.
(82) Yoo, H. D.; Markevich, E.; Salitra, G.; Sharon, D.; Aurbach, D. On the challenge of developing advanced technologies for electrochemical energy storage and conversion. *Mater. Today* **2014**, *17*, 110−121.
(83) Yariv, O.; Hirshberg, D.; Zinigrad, E.; Meitav, A.; Aurbach, D.; Jiang, M.; Powell, B. R. Carbon negative electrodes for Li-ion batteries: The effect of solutions and temperatures. *J. Electrochem. Soc.* **2014**, *161*, A1422−A1431.
(84) Lotfabad, E. M.; Kalisvaart, P.; Kohandehghan, A.; Cui, K.; Kupsta, M.; Farbod, B.; Mitlin, D. Si nanotubes ALD coated with TiO_2, TiN or Al_2O_3 as high performance lithium ion battery anodes. *J. Mater. Chem. A* **2014**, *2*, 2504−2516.
(85) Zheng, J.; Yan, P.; Kan, W. H.; Wang, C.; Manthiram, A. A spinel-integrated P2-type layered composite: High-rate cathode for sodium-ion batteries. *J. Electrochem. Soc.* **2016**, *163*, A584−A591.
(86) Cosandey, F.; Su, D.; Sina, M.; Pereira, N.; Amatucci, G. G. Amatucci, G. G. Fe valence determination and Li elemental distribution in lithiated $FeO_{0.7}F_{1.3}$/C nanocomposite battery materials by electron energy loss spectroscopy (EELS). *Micron* **2012**, *43*, 22−29.
(87) Cosandey, F.; Sina, M.; Su, D.; Pereira, N.; Amatucci, G. EELS Determination of Li Distribution and Fe Valence Mapping in Lithiated FeOF/C Nanocomposite Battery Materials. *Microsc. Microanal.* **2011**, *17*, 1586−1587.
(88) Andersson, A. S.; Thomas, J. O. The source of first-cycle capacity loss in $LiFePO_4$. *J. Power Sources* **2001**, *97*−*98*, 498−502.
(89) Delmas, C.; Maccario, M.; Croguennec, L.; Le Cras, F.; Weill, F. Lithium deintercalation in $LiFePO_4$ nanoparticles via a domino-cascade model. *Nat. Mater.* **2008**, *7*, 665−671.
(90) Dedryvère, R.; Maccario, M.; Croguennec, L.; Le Cras, F.; Delmas, C.; Gonbeau, D. X-ray photoelectron spectroscopy investigations of carbon-coated $LixFePO_4$ materials. *Chem. Mater.* **2008**, *20*, 7164−7170.
(91) El Ouatani, L.; Dedryvère, R.; Siret, C.; Biensan, P.; Gonbeau, D. Effect of vinylene carbonate additive in Li-ion batteries: Comparison of $LiCoO_2$/C, $LiFePO_4$/C, and $LiCoO_2/Li_4Ti_5O_{12}$ systems. *J. Electrochem. Soc.* **2009**, *156*, A468−A477.
(92) Shi, J.; Wang, Z.; Fu, Y. Density functional theory study of lithium diffusion at the interface between olivine-type $LiFePO_4$ and $LiMnPO_4$. *J. Phys. D: Appl. Phys.* **2016**, *49*, 505601.
(93) Tang, K.; Yu, X.; Sun, J.; Li, H.; Huang, X. Kinetic analysis on $LiFePO_4$ thin films by CV, GITT, and EIS. *Electrochim. Acta* **2011**, *56*, 4869−4875.
(94) Trócoli, R.; Franger, S.; Cruz, M.; Morales, J.; Santos-Pena, J. Improving the electrochemical properties of nanosized $LiFePO_4$-based electrode by boron doping. *Electrochim. Acta* **2014**, *135*, 558−567.
(95) Lai, Y.; Cao, Z.; Song, H.; Zhang, Z.; Chen, X.; Lu, H.; Jia, M.; Li, J. Influence of Fe (II) species in electrolyte on performance of graphite anode for lithium-ion batteries. *J. Electrochem. Soc.* **2012**, *159*, A1961−A1966.
(96) Li, X.; Zheng, J.; Ren, X.; Engelhard, M. H.; Zhao, W.; Li, Q.; Zhang, J.-G.; Xu, W. Dendrite-free and performance-enhanced lithium metal batteries through optimizing solvent compositions and adding combinational additives. *Adv. Energy Mater.* **2018**, *8*, 1703022.

https://dx.doi.org/10.1021/acs.jpclett.0c00317
J. Phys. Chem. Lett. 2020, 11, 4608−4617